EUROPEAN ORGANIZATION FOR NUCLEAR RESEARCH

HIGH ENERGY Pb+Pb COLLISIONS VIEWED BY PION INTERFEROMETRY

I.G. Bearden[1], H. Bøggild[1], J. Boissevain[2], J. Dodd[3], B. Erazmus[4],
S. Esumi[5,b], C.W. Fabjan[6], D. Ferenc[7], D.E. Fields[2,c], A. Franz[6,d],
J. Gaardhøje[1], M. Hamelin[10], A.G. Hansen[1], O. Hansen[1], D. Hardtke[8,g],
H. van Hecke[2], E.B. Holzer[6], T.J. Humanic[8], P. Hummel[6], B.V. Jacak[11],
R. Jayanti[8], K. Kaimi[5], M. Kaneta[5], T. Kohama[5], M. Kopytine[11],
M. Leltchouk[3], A. Ljubičić, Jr.[7,d], B. Lörstad[9], N. Maeda[5,e],
R. Malina[6], A. Medvedev[3], M. Murray[10], H. Ohnishi[5], G. Paić[8],
S.U. Pandey[8,f], F. Piuz[6], J. Pluta[4], V. Polychronakos[12], M. Potekhin[3],
G. Poulard[6], D. Reichhold[8], A. Sakaguchi[5,a], J. Simon-Gillo[2],
J. Schmidt-Sørensen[9], W. Sondheim[2], M. Spegel[6], T. Sugitate[5],
J.P. Sullivan[2], Y. Sumi[5], W.J. Willis[3], K.L. Wolf[10],
N. Xu[2,g], and D.S. Zachary[8]

Abstract

Two-pion correlations from Pb+Pb collisions at 158 GeV/c per nucleon are measured by the NA44 experiment at CERN. Multidimensional fits characterize the emission volume, which is found to be larger than in S-induced collisions. Comparison with the RQMD model is used to relate the fit parameters to the actual emission volume.

[1] Niels Bohr Institute, DK-2100, Copenhagen, Denmark.

[2] Los Alamos National Laboratory, Los Alamos, NM 87545, USA.

[3] Columbia University, New York, NY 10027, USA.

[4] Nuclear Physics Laboratory of Nantes, 44072 Nantes, France.

[5] Hiroshima University, Higashi-Hiroshima 739, Japan.

[6] CERN, CH-1211 Geneva 23, Switzerland.

[7] Rudjer Boskovic Institute, Zagreb, Croatia.

[8] Ohio State University, Columbus, OH 43210, USA.

[9] University of Lund, S-22362 Lund, Sweden.

[10] Texas A&M University, College Station, TX 77843, USA.

[11] State University of New York, Stony Brook, NY 11794, USA.

[12] Brookhaven National Laboratory, Upton, NY 11973, USA.

[a] Now at Osaka University, Toyonaka, Osaka 560-0043, Japan.

[b] Now at Heidelberg University, D-69120 Heidelberg, Germany.

[c] Now at University of New Mexico, Albuquerque, NM 87131, USA.

[d] Now at Brookhaven National Laboratory, Upton, NY 11973, USA.

[e] Now at Florida State University, Tallahassee, FL 32306, USA.

[f] Now at Wayne State University, Detroit, MI 48202, USA.

[g] Now at Lawrence Berkeley National Laboratory, Berkeley, CA 94720, USA.

1   Introduction

Two-particle intensity interferometry has been used to provide information on the space–time extent of the particle-emitting source in heavy-ion collisions [1, 2, 3, 4], and has been shown to be sensitive to the collision dynamics [2, 5]. If a first-order phase transition from a quark–gluon plasma is present the duration of particle emission can be comparable to the spatial extent of the source [6, 7]. The duration of particle emission may be measurable through a multidimensional analysis of the two-particle correlation function, although the expansion dynamics of the particle-emitting source and final-state interactions complicate the interpretation [8]. The transverse-momentum dependence of the correlation function gives insight into the dynamics of the system as well as the resonance decay contributions to the particle sample [9]. The two-particle correlation data can be coupled with inclusive particle yields and spectra to provide constraints on source parameters such as temperature and radial-flow velocity [10].

Pb beams from the CERN SPS, accelerated to 158 GeV/c per nucleon colliding with a Pb target create the heaviest system at the highest energy density ever produced in the laboratory. Central Pb+Pb collisions produce more secondary particles than any nuclear collisions studied previously. Consequently, we may naïvely expect significantly larger source sizes than seen in S+Pb collisions at 200 GeV/c per nucleon, and can investigate whether the Pb+Pb system is longer lived or has a higher transverse expansion velocity. The NA44 experiment has measured distributions and correlations of identical particles, which can be used to characterize this system and search for evidence of a phase transition.

This paper reports the $\pi^+\pi^+$ and $\pi^-\pi^-$ correlation function analysis. The $\pi^+\pi^+$ correlation analysis is performed as a function of pair transverse mass ($m_{\mathrm{T}}^2 = p_{\mathrm{T}}^2 + m^2$), yielding insight into the expansion dynamics of the source and the resonance contribution to the pion sample.

2   Experiment and data analysis

Experiment NA44 is a focusing spectrometer measuring particle distributions at midrapidity with excellent particle identification. Figure 1 shows the spectrometer set-up. The NA44 acceptance is optimized for particle pairs with small momentum differ-ence, allowing small statistical uncertainties in the correlation function in the region of the Bose–Einstein correlations. Two dipole magnets (D1 and D2) and three quadrupoles (Q1, Q2, and Q3) create a magnified image of the target in the spectrometer [11]. One charge sign at a time is detected. The momentum range in this analysis covers a band of ± 20% about the nominal momentum setting of 4 GeV/c. Two angular settings of the spectrometer with respect to the beam axis are used, 44 and 131 mrad, and re-ferred to as the low-p_{T} ($\sim$ 170 MeV/c) and high-p_{T} ($\sim$ 480 MeV/c) settings, respectively. The laboratory rapidity (y) and p_{T} range is y = 3.1–4.1, p_{T} = 0–0.4 GeV/c for the low-p_{T} pions and y = 2.5–3.1, p_{T} = 0.3–0.8 GeV/c for the high-p_{T} setting. The rapid-ity of the incident Pb projectile is 5.8. Two focus settings of the quadrupoles, called horizontal and vertical, optimize the acceptance for different components of the two-particle momentum difference ($\vec{Q}$). The rapidity and transverse momentum ranges of

1

the acceptances for the 44 mrad and 131 mrad horizontal and vertical settings are shown in Fig. 2. The momentum resolution of the spectrometer is $\sigma \approx 10$ MeV; the Q resolution is $\sigma \approx 15$ MeV.
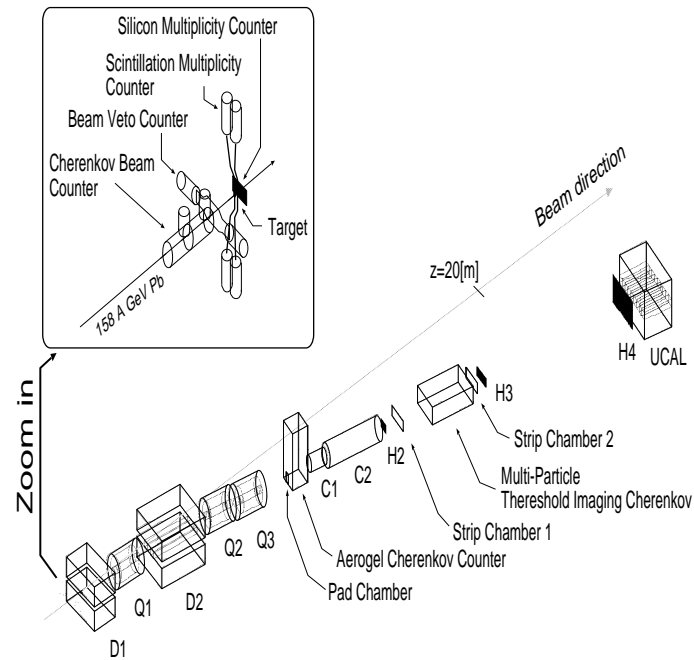

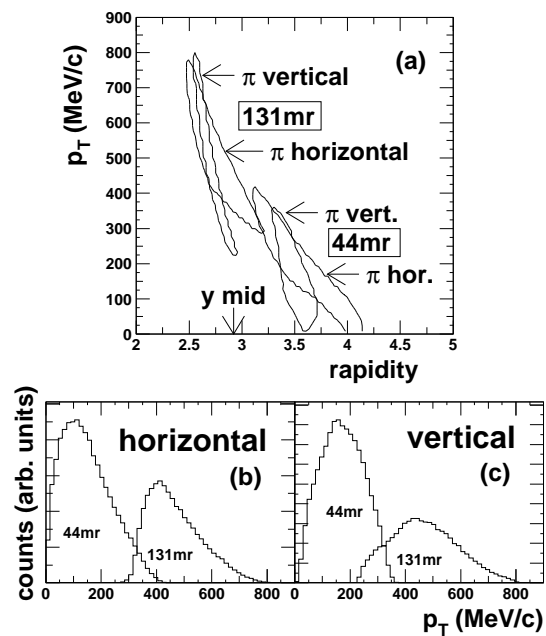Figure 1: The NA44 spectrometer in 1995 and 1996.

Figure 2: The NA44 pion acceptance for the 4 GeV/c 44 mrad and 131 mrad horizontal and vertical settings.

2

Particles are detected and identified using a Cherenkov – pad chamber – time-of-flight (TOF) complex. Tracks are reconstructed using straight-line fits to the hits on two highly segmented scintillator hodoscopes (H2 and H3), a pad chamber (PC) and two strip chambers (SC1 and SC2). The TOF start signal is derived from a beam counter with a time resolution of $\sigma \approx 35$ ps [12]. Particle identification in this analysis uses TOF from the hodoscopes (resolution $\sigma \approx 100$ ps) and Cherenkov information. Events with electrons in the spectrometer are vetoed at the trigger level using a threshold Cherenkov detector (C2). Offline, events with at least two pions are selected by requiring a sufficient ADC signal in a second threshold gas Cherenkov counter (C1). In addition the combination of TOF and momentum for the individual tracks is used to construct the square of the mass for individual tracks. A threshold imaging Cherenkov (TIC) [13] distinguishes pions from heavier particles on a track-by-track basis. The TIC signal is used in conjunction with the hodoscope information to select the pions used in this analysis. The residual contamination from particles other than pions is typically less than 1%.

The NA44 pairs trigger requires a valid beam particle, and at least two hits on both H2 and H3. Central Pb+Pb collisions were selected by means of a threshold on a scintillator downstream of the target, covering the pseudorapidity range $1.3 \leq \eta \leq 3.5$. The trigger centralities, target thickness, and final number of pion pairs used in this analysis are listed in Table 1. The error on the centrality is $\pm 1\%$.

Table 1: The particle species, spectrometer angle (in mrad), quadrupole focus, Pb-target thickness (in g/cm^2), trigger centrality ($\sigma_{\text{trig}}/\sigma_{\text{total}}$ in %), and number of valid pion pairs for the data sets used in these analyses. A Pb-target thickness of 1.14 (2.27) g/cm^2 is approximately 2.1 (4.2)% of an interaction length for a projectile.

	Angle	Focus	Target thickness	Centrality	No. of pairs (10^3)
$\pi^-\pi^-$	44	horizontal	2.27 gm/cm^2	18%	171
		vertical	2.27 gm/cm^2	18%	149
$\pi^+\pi^+$	44	horizontal	1.14 gm/cm^2	15%	140
		vertical	1.14 gm/cm^2	15%	106
$\pi^+\pi^+$	131	horizontal	1.14 gm/cm^2	15%	104
		vertical	2.27 gm/cm^2	18%	84

We present fits in one dimension, $Q_{\text{inv}} = \sqrt{\vec{Q}^2 - Q_0^2}$, as well as in three dimensions. Q_{L} is parallel to the beam, while the direction perpendicular to the beam is resolved into a direction along the momentum sum of the particles, Q_{TO}, and a direction perpendicular to this, Q_{TS}. Being parallel to the velocities of the particles, Q_{TO} is sensitive to the duration of particle emission [6, 7]. Data are analysed in the longitudinally co-moving system (LCMS) frame, in which the momentum sum in the beam direction of both particles is zero. In this frame, the Q_{TO} direction corresponds closely to the direction coming straight from the source in the rest frame of the source [14].

The raw correlation function is

$$C_{\text{raw}}(\vec{k}_1, \vec{k}_2) = \frac{R(\vec{k}_1, \vec{k}_2)}{B(\vec{k}_1, \vec{k}_2)} \tag{1}$$

3

where $\vec{k}_i$ are the particle momenta, $R(\vec{k}_1, \vec{k}_2)$ is the 'real distribution' of pion-pair relative momenta in the recorded events, and $B(\vec{k}_1, \vec{k}_2)$ is the 'background distribution' generated using mixed events from the same data sample. The background is generated by randomly selecting ten pairs of events for each real event; in these background pairs, one particle in each event is selected randomly to create a fake 'event' for the background distribution. Consequently the statistical error is dominated by the real data sample. The background track pairs are subject to the same analysis procedure and cuts as the real pairs.

The background spectrum is distorted compared to the true uncorrelated two-particle spectrum owing to the effect of the two-particle correlations on the single-particle spectrum [15], and the data are corrected for this. Two-particle correlations arising from Coulomb interactions are corrected for using either a Coulomb wave-function integration [16] or Gamow correction. The Gamow correction is the limit of the Coulomb wave-function integration for a point source. Coulomb interactions with the residual nuclear system are neglected. The correction procedures are described in more detail in Ref. [11].

Corrections for the finite momentum resolution and two-particle acceptance of the spectrometer are made using a Monte Carlo procedure [1, 11]. The Monte Carlo incorporates a detailed description of the spectrometer response, including all tracking chambers. Two-particle events are generated from an exponential transverse-mass distribution and propagated through the detector simulation. The tracks are then fitted using the same reconstruction procedure used with the real data. The correction procedure uses only Monte Carlo events with two valid tracks after reconstruction: For these events there are two input momenta $(\vec{k}_1, \vec{k}_2)$ and two reconstructed momenta $(\vec{k}_1', \vec{k}_2')$. The acceptance and momentum resolution correction is then

$$K_{\text{acceptance}} = \frac{C_2(\text{ideal})}{C_2(\text{reconstructed})} = \frac{[R(\vec{k}_1, \vec{k}_2)]/[B(\vec{k}_1, \vec{k}_2)]}{[R(\vec{k}_1', \vec{k}_2')]/[B(\vec{k}_1', \vec{k}_2')]}, \tag{2}$$

where $R(\vec{k}_1, \vec{k}_2)$ is the real distribution of simulated events weighted by the Bose–Einstein correlation, $B(\vec{k}_1, \vec{k}_2)$ is the background distribution of simulated events, $R(\vec{k}_1', \vec{k}_2')$ is the distribution of reconstructed Monte Carlo events weighted by the Bose–Einstein correlation and subject to the same analysis cuts as the real data, and $B(\vec{k}_1', \vec{k}_2')$ is formed from mixed, reconstructed Monte Carlo events and is subject to the same analysis cuts as the real data. $B(\vec{k}_1', \vec{k}_2')$ is corrected for the fact that in the real data the Coulomb correction has been applied to data which have been measured with a finite momentum resolution.

One-dimensional and three-dimensional fits are performed. For the one-dimensional fits, only data from the horizontal setting are used and the data are fitted with:

$$C(Q_{\text{inv}}) = D(1 + \lambda e^{-Q_{\text{inv}}^2 R_{\text{inv}}^2}). \tag{3}$$

In the three-dimensional case, two different Gaussian parametrizations are utilized:

$$C(Q_{\text{TO}}, Q_{\text{TS}}, Q_{\text{L}}) = D(1 + \lambda e^{-Q_{\text{TO}}^2 R_{\text{TO}}^2 - Q_{\text{TS}}^2 R_{\text{TS}}^2 - Q_{\text{L}}^2 R_{\text{L}}^2}), \tag{4}$$

and

$$C(Q_{\text{TO}}, Q_{\text{TS}}, Q_{\text{L}}) = D(1 + \lambda e^{-Q_{\text{TO}}^2 R_{\text{TO}}^2 - Q_{\text{TS}}^2 R_{\text{TS}}^2 - Q_{\text{L}}^2 R_{\text{L}}^2 - 2Q_{\text{TO}} Q_{\text{L}} R_{\text{OL}}^2}) . \tag{5}$$

4

R_{OL}^2 is the 'out-longitudinal' cross term [17] which can be positive or negative. For the three-dimensional fits without the cross term, only the magnitudes of the momentum differences are used. When doing a cross-term fit, Q_{TO} and Q_{TS} are defined to be positive, and Q_{L} is allowed to be positive or negative. For the three-dimensional fits, data from the horizontal and vertical spectrometer settings are fitted simultaneously. The Coulomb wave-function integration, background correction, and acceptance correction depend on the source size so an iterative approach with a Gaussian source distribution is used. The fits converge inside the experimental statistical error within five iterations.

The fitted radius and lambda parameters presented here are found by minimizing [1]

$$\chi^2 = \sum_{i,j}(C_i - R_i/B_i)V_{ij}^{-1}(C_j - R_j/B_j) \tag{6}$$

where R_i is the real distribution, B_i is the background distribution, C_i is the fit function, V_{ij} is the covariance matrix, and i, j are indices for different data points. Only bins with at least 100 counts in the background and 30 counts in the reals were used in the fitting process. The error matrix includes both statistical and systematic errors. The systematic errors were evaluated by varying the analysis parameters. These variations include changing the momentum resolution assumed in the Monte Carlo correction by $\pm 20\%$, changing the minimum two-track separation cuts at the pad chamber and hodoscope 2, changing the minimum number of strip-chamber hits for a valid pair, and allowing the horizontal and vertical data to have different λ parameters during the iterative correction procedure. The systematic error matrix is calculated from

$$V_{ij}^{\mathrm{sys}} = [\frac{\sum_{k=1}^{N} C_{ik}C_{jk}}{N} - C_i^{\mathrm{mean}}C_j^{\mathrm{mean}}]\frac{N}{N-1} \tag{7}$$

where N is the number of fits performed with different analysis parameters and cuts. The total error matrix is

$$V_{ij} = V_{ij}^{\mathrm{sys}} + V_{ij}^{\mathrm{stat}}; \quad V_{ij}^{\mathrm{stat}} = 0 \text{ if } i \neq j. \tag{8}$$

Maximum likelihood fits were also performed but are not presented owing to the difficulty in including systematic errors in the maximum likelihood fit. The parameters from χ^2 and maximum likelihood fits were found to be nearly identical. When making the maximum likelihood fits, the cuts on the number of counts per bin were varied — the resulting fit parameters were insensitive to these cuts.

3 Results

The one-dimensional fits and projections of the three-dimensional fits onto the three axes are shown together with the Coulomb-wave corrected Pb+Pb data in Fig. 3. For the three-dimensional projections, the data from the horizontal and vertical settings are both shown. The top row shows the correlation function and fit for the low-p_{T} $\pi^-\pi^-$ data, the middle row shows the low-p_{T} $\pi^+\pi^+$ data, and the bottom row shows the high-p_{T} $\pi^+\pi^+$ data.
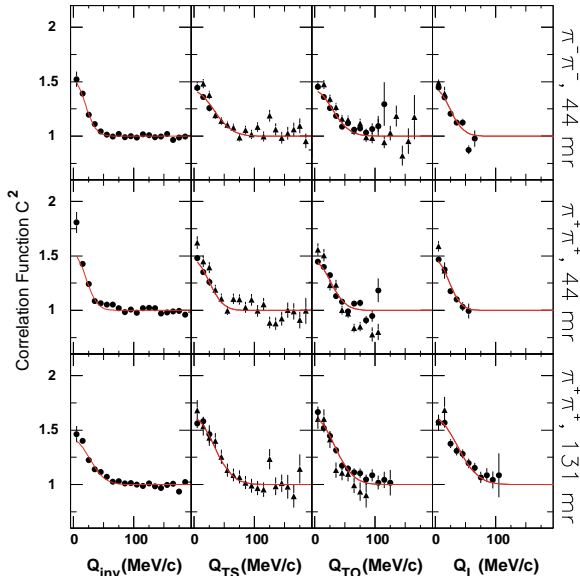
Figure 3: The one-dimensional correlation functions and the projections of the three-dimensional correlation functions for the 44 mrad $\pi^-\pi^-$, 44 mrad $\pi^+\pi^+$ and the 131 mrad $\pi^+\pi^+$ data. Also included are the projections of the fitted Gaussian parametrizations. The projections are over the lowest 20 MeV/c in the other momentum-difference directions. The solid circles are the data from the horizontal setting and the solid triangles are the data from the vertical setting. The data shown here use the Coulomb wave-function integration correction.

The extracted source parameters from Gaussian fits to the Gamow-corrected correlation functions are given in Tables 2 and 3, and compared to those from S+Pb collisions. The S+Pb results come from the most central 3% of collisions. Tables 4 and 5 give the extracted source parameters when the Coulomb wave-function correction is used. Table 5 also gives the extracted fit parameters when the R^2_{OL} cross term is included in the fit function.

Table 2: Fitted results of Gaussian parametrizations of the $\pi^+\pi^+$ and $\pi^-\pi^-$ correlation functions in Q_{inv}. Both the S+Pb and Pb+Pb data are Gamow-corrected. Errors are statistical+systematic. The S+Pb results are taken from Refs. [1, 5] ($\langle p_{\mathrm{T}} \rangle$ in MeV/c).

System	λ	R_{inv} (fm)	$\chi^2/$dof
PbPb $\pi^-\pi^-(\approx 170)$	0.556 ± 0.033	6.62 ± 0.29	$32/36$
PbPb $\pi^+\pi^+(\approx 170)$	0.536 ± 0.040	6.06 ± 0.31	$61/27$
PbPb $\pi^+\pi^+(\approx 480)$	0.446 ± 0.029	4.94 ± 0.28	$56/35$
SPb $\quad\pi^-\pi^-(\approx 150)$	0.42 ± 0.02	4.00 ± 0.27	$19/25$
SPb $\quad\pi^+\pi^+(\approx 150)$	0.56 ± 0.02	5.00 ± 0.22	$29/25$
SPb $\quad\pi^+\pi^+(\approx 450)$	0.48 ± 0.02	4.27 ± 0.23	$27/20$

Table 3: Fitted results of Gaussian parametrizations of the $\pi^+\pi^+$ and $\pi^-\pi^-$ correlation functions in Q_{TO}, Q_{TS} and Q_{L}. Both the S+Pb and Pb+Pb data are Gamow-corrected. Errors are statistical+systematic. The S+Pb results are taken from [1, 5] ($\langle p_{\mathrm{T}}\rangle$ in MeV/c).

System	λ	R_{TO} (fm)	R_{TS} (fm)	R_{L} (fm)	χ^2/dof
PbPb $\pi^-\pi^-(\approx 170)$	0.526 ± 0.022	4.36 ± 0.18	4.09 ± 0.26	5.55 ± 0.30	$1684/2105$
PbPb $\pi^+\pi^+(\approx 170)$	0.591 ± 0.031	4.82 ± 0.21	5.36 ± 0.48	5.94 ± 0.40	$1442/1720$
PbPb $\pi^+\pi^+(\approx 480)$	0.707 ± 0.033	4.06 ± 0.16	4.21 ± 0.28	3.75 ± 0.20	$1124/1574$
SPb $\pi^+\pi^+(\approx 150)$	0.56 ± 0.02	4.02 ± 0.14	4.15 ± 0.27	4.73 ± 0.26	$1201/1415$
SPb $\pi^+\pi^+(\approx 450)$	0.55 ± 0.02	2.97 ± 0.16	2.95 ± 0.24	3.09 ± 0.19	$1500/1095$

Table 4: Fitted results of Gaussian parametrizations of the $\pi^+\pi^+$ and $\pi^-\pi^-$ correlation functions in Q_{inv} using the Coulomb-wave correction. Errors are statistical+systematic ($\langle p_{\mathrm{T}}\rangle$ in MeV/c).

System	λ	R_{inv} (fm)	χ^2/dof
PbPb $\pi^-\pi^-(\approx 170)$	0.517 ± 0.040	7.56 ± 0.38	$30/36$
PbPb $\pi^+\pi^+(\approx 170)$	0.519 ± 0.048	7.16 ± 0.42	$52/27$
PbPb $\pi^+\pi^+(\approx 480)$	0.407 ± 0.031	5.39 ± 0.36	$51/35$

Table 5: Fitted results of Gaussian parametrizations of the $\pi^+\pi^+$ and $\pi^-\pi^-$ correlation functions in Q_{TO}, Q_{TS} and Q_{L} using the Coulomb-wave correction. The fitted results with and without the R^2_{OL} cross term are shown. Errors are statistical+systematic ($\langle p_{\mathrm{T}}\rangle$ in MeV/c).

System	λ	R_{TO} (fm)	R_{TS} (fm)	R_{L} (fm)	R^2_{OL} (fm^2)	χ^2/dof
PbPb $\pi^-\pi^-(\approx 170)$	0.495 ± 0.023	4.88 ± 0.21	4.45 ± 0.32	6.03 ± 0.35	–	$1683/2105$
PbPb $\pi^+\pi^+(\approx 170)$	0.569 ± 0.035	5.50 ± 0.26	5.87 ± 0.58	6.58 ± 0.48	–	$1423/1720$
PbPb $\pi^+\pi^+(\approx 480)$	0.679 ± 0.034	4.39 ± 0.18	4.39 ± 0.31	3.96 ± 0.23	–	$1125/1574$
PbPb $\pi^-\pi^-(\approx 170)$	0.524 ± 0.026	5.35 ± 0.25	5.07 ± 0.35	6.68 ± 0.39	10.7 ± 2.9	$1822/2279$
PbPb $\pi^+\pi^+(\approx 170)$	0.658 ± 0.035	5.98 ± 0.23	6.94 ± 0.48	7.39 ± 0.40	28.1 ± 3.5	$1746/1786$
PbPb $\pi^+\pi^+(\approx 480)$	0.693 ± 0.037	4.59 ± 0.21	4.71 ± 0.36	4.15 ± 0.25	3.1 ± 1.4	$1187/1655$

Figure 4 compares the Gamow-corrected and Coulomb-wave corrected data and fits for the low-p_{T} $\pi^-\pi^-$ setting. In these plots, the projections in Q_{TO} and Q_{L} come from the horizontal setting and the projection in Q_{TS} comes from the vertical setting. For extended sources, the Gamow factor, which is the point-source approximation, over-predicts the Coulomb repulsion between a pair of charged particles. Comparing the results from the three-dimensional fits listed in Tables 3 and 5 we see that using the Gamow factor reduces the measured radius parameters by 8–12% for the low-p_{T} cases and by 4–8% for the high-p_{T} case. The λ parameters from the 3D data are larger by 3–6% when the Gamow correction is used. All of the changes are consistent with the overcorrection we expect from the Gamow correction.
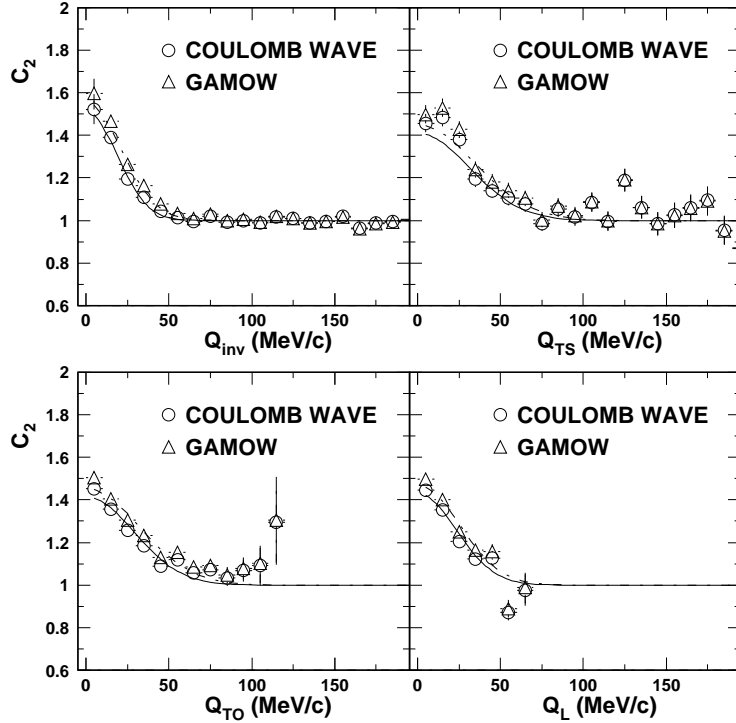
Figure 4: Comparison of the Coulomb-wave and Gamow-corrected 44 mrad $\pi^-\pi^-$ data. The Q_{inv} data and the Q_{TO} and Q_{L} projections are from the horizontal setting, and the Q_{TS} projection is from the vertical setting. The three-dimensional projections are averaged over the lowest 20 MeV/c in the other momentum differences.

The fit parameters from the three-dimensional fits to the positive-pion data without the R_{OL}^2 cross term are plotted in Fig. 5 as a function of the mean transverse mass. Also plotted in Fig. 5 is the fit of the R_{L} radius parameter to the function $R_{\text{L}} = A/\sqrt{m_{\text{T}}}$. The fitted value of A is 2.9 fm·GeV$^{1/2}$. There is a difference in the rapidity of the high-m_{T} ($\langle y \rangle \approx 2.8$) and low-$m_{\text{T}}$($\approx 3.6$) points, which has been ignored in this fit. We observed that in S+Pb collisions the radius parameters follow a common $1/\sqrt{m_{\text{T}}}$ scaling [5]. As can be seen in Fig. 5, the radius parameters decrease with increasing m_{T}, but common m_{T} scaling is no longer the case. The R_{L} and R_{TS} radius parameters are consistent with $1/\sqrt{m_{\text{T}}}$ scaling, but the R_{TO} radius parameters are not. The fitted three-dimensional λ parameter increases with increasing m_{T} as would be expected from a reduced resonance contribution to the high-p_{T} pion sample.

The fitted three-dimensional radius parameters for low-p_{T} $\pi^-\pi^-$ data are somewhat smaller than those for the low-p_{T} $\pi^+\pi^+$. It is important to note that the λ parameter is strongly correlated with the radius parameters, and the fitted λ for $\pi^-\pi^-$ is smaller than that for $\pi^+\pi^+$. Consequently, comparison of the fit parameters may overemphasize differences between data sets. In order to test whether this difference in the radius parameters for negative and positive pions is significant, we overlay the correlation functions
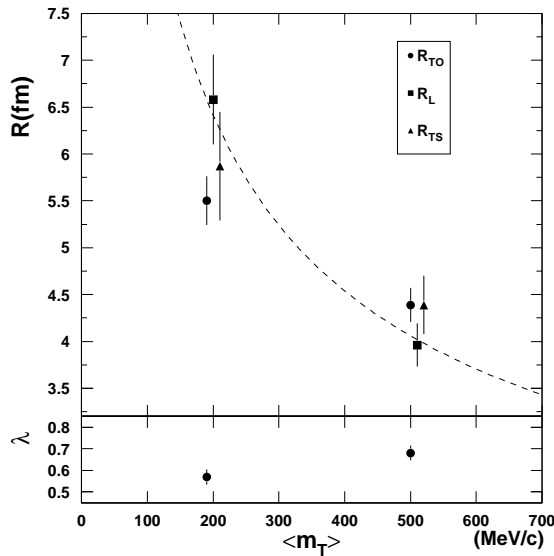
8

Figure 5: The m_T dependence of $\pi^+\pi^+$ radius and λ parameters. Also included is the fit of the R_L radius parameters to the function $A/\sqrt{m_\mathrm{T}}$.

in Fig. 6 and calculate a χ^2 difference per degree of freedom between the two data sets. This calculation uses bins in which $|Q_\mathrm{TS}|, |Q_\mathrm{TO}|, |Q_\mathrm{L}| < 80$ MeV/c; the χ^2 difference per degree of freedom in this region is $450/440$. As this is nearly unity, we must conclude that the $\pi^+\pi^+$ and $\pi^-\pi^-$ correlations do not, in fact, differ. In contrast, the χ^2 difference between low- and high-p_T $\pi^+\pi^+$ data sets in the same region of $\vec{Q}$-space is $518/371$. This study illustrates an important limitation to using only the fitted parameters to compare data sets. The problems are certainly exacerbated when comparing data from different experiments where statistical and systematic errors depend differently upon $\vec{Q}$. In addition, this emphasizes the need to compare the correlation functions derived from models directly with the data and not simply to compare the extracted radius parameters.

The R_OL^2 cross term is non-zero for all data sets, and is rather large for the low-p_T $\pi^+\pi^+$ data. It was predicted that in the LCMS frame the R_OL^2 cross term should be non-zero if the source is not symmetric under a reflection about $z = 0$, where z is defined as the beam axis [17]. Since the NA44 low-p_T setting is slightly forward of midrapidity ($\langle y \rangle \approx 3.6$), this condition of reflection symmetry is not fulfilled. Comparing the fitted results with and without the R_OL^2 cross term, all radius and λ parameters become larger when the cross term is included in the fit. The cross term can also be expressed [18] in terms of a linear 'out-longitudinal' correlation coefficient, ρ_ol, and the R_TO and R_L parameters: $R_\mathrm{OL}^2 \equiv -\rho_\mathrm{ol} R_\mathrm{TO} R_\mathrm{L}$. If ρ_ol is calculated from the fit parameters in Table 5, the magnitudes are all less than one, as expected. The results show a stronger correlation between Q_TO and Q_L for the low-p_T setting ($\rho_\mathrm{ol} = -0.64 \pm 0.09$ for π^+ and -0.29 ± 0.08 for π^-) and weaker correlation between Q_TO and Q_L for the high-p_T π^+ data ($\rho_\mathrm{ol} = -0.16 \pm 0.07$). A small ρ_ol value is expected for the high-p_T setting since it is close to midrapidity and ρ_ol

9
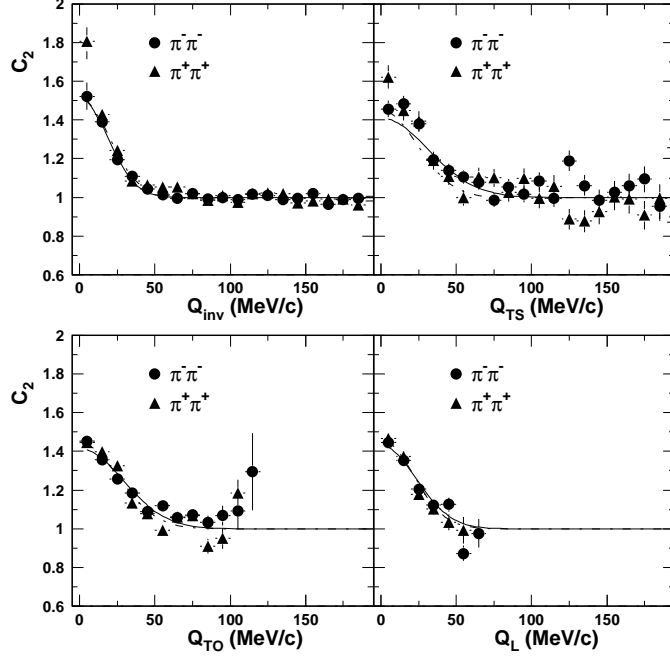
Figure 6: Comparison of NA44 44-mrad $\pi^-\pi^-$ and $\pi^+\pi^+$ data. The Q_{inv} data and the Q_{TO} and Q_{L} projections are from the horizontal setting, and the Q_{TS} projection is from the vertical setting. The three-dimensional projections are averaged over the lowest 20 MeV/c in the other momentum differences.

is expected to be zero at midrapidity (where it changes sign). The difference between the ρ_{ol} values for π^+ and π^- (0.35 ± 0.12) seems significant, but the direct comparison of the π^+ and π^- correlation functions (see text above and Fig. 6) suggests the two correlation functions are not significantly different.

The R parameters from Pb+Pb collisions are larger than those in S+Pb collisions. This may be naïvely expected from the larger initial source size with the Pb projectile, but we note that the R parameters do not directly reflect the size of the emitting source [5, 8]. The ratio of Pb to S nuclear radii is 1.87, which is larger than the ratio of the observed R parameters. In Pb+Pb collisions, the R_{L} parameter is larger than the two transverse R parameters for the both low-p_{T} $\pi^+\pi^+$ and low-p_{T} $\pi^-\pi^-$ data. This was not visible in S+Pb [1, 2] or S+S collisions [2].

The duration of particle emission ($\Delta\tau$) can be estimated using the formula [6, 7, 19] $c\Delta\tau = \sqrt{(R_{\mathrm{TO}}^2 - R_{\mathrm{TS}}^2)}/\beta$, where β is the transverse velocity of the pion pair. In the Pb+Pb data, the two transverse-radius parameters are similar for all cases – which appears to be inconsistent with a long duration of a mixed (hadronic–partonic) phase during which pions are emitted. However, for an expanding source, the above formula can underestimate the duration of pion emission for values of p_{T} above about 100 MeV/c [8]. For such a source, a particle's freeze-out position and momentum are correlated, violating the assumptions made in deriving the formula for $\Delta\tau$.

10

4   Discussion

The radius parameter values do not yield the actual source size as expansion-induced correlations between the particle position and momentum limit the sensitivity to only part of the emitting source [5, 8]. However, the larger radius parameters in Pb+Pb compared to S+Pb collisions do reflect a larger size at freeze-out as well as a larger initial source. This result shows that predictions of sensitivity only to a thermal length scale are not borne out [20].

The ratio of radius parameters for Pb+Pb to S+Pb collisions is smaller than the ratio of the nuclear radii. This may indicate that the Pb+Pb radius parameters are more modified by expansion than those from S+Pb. However, the S+Pb results were for the most central 3% of collisions, and the Pb+Pb interferometry results presented here are for semi-central collisions (see Table 1).

We compare the experimental results with calculations [14, 21] based on the RQMD event generator [22] and a filter simulating the acceptance of NA44. RQMD (Version 1.08) simulates the space–time evolution of heavy-ion collisions, including rescattering of the produced particles and the production and decay of resonances. Figure 7 compares the shape of the $\pi^-\pi^-$ and $\pi^+\pi^+$ correlation functions from generator and data; the RQMD events are selected on event multiplicity to match the NA44 trigger. The fit parameters from RQMD are listed in Tables 6 and 7. For the one-dimensional parametrizations RQMD predicts much larger R_{inv} radius parameters than observed in the data (27–37%). A direct comparison of the one-dimensional correlation functions in Fig. 7 shows that this difference is mainly caused by differences in data and RQMD for the lowest bin in momentum difference. For the three-dimensional parametrizations of the the low-p_{T} $\pi^-\pi^-$ and $\pi^+\pi^+$ data, RQMD predicts radius parameters that are slightly larger than the measured radius parameters. The discrepancy between data and RQMD is larger for the $\pi^-\pi^-$ measurement than the $\pi^+\pi^+$ measurement: RQMD predicts that the radius parameters should be larger for $\pi^-\pi^-$. RQMD shows the same trend as the data where R_{L} is larger than the transverse R parameters for the low-p_{T} correlation functions. For the high-p_{T} $\pi^+\pi^+$ data, RQMD predicts radius parameters that are similar to the measured radius parameters, but it significantly overpredicts the value of the λ parameter. RQMD does reproduce the result that the one-dimensional parametrization of the high-p_{T} $\pi^+\pi^+$ correlation functions gives a λ parameter that is smaller than the λ parameter from the three-dimensional parametrization. For both the NA44 data and the RQMD calculations, this discrepancy is probably due to the fact that a Gaussian parametrization is used for one-dimensional correlation functions that are non-Gaussian (as demonstrated by the large χ^2/dof).

Table 6: Fitted results of Gaussian parametrizations of the RQMD $\pi^+\pi^+$ and $\pi^-\pi^-$ correlation functions in Q_{inv} ($\langle p_{\mathrm{T}} \rangle$ in MeV/c).

System	λ	R_{inv} (fm)	χ^2/N
PbPb $\pi^-\pi^-(\approx 170)$	0.58 ± 0.02	9.96 ± 0.29	11.0
PbPb $\pi^+\pi^+(\approx 170)$	0.67 ± 0.02	9.06 ± 0.21	8.6
PbPb $\pi^+\pi^+(\approx 480)$	0.59 ± 0.05	7.36 ± 0.48	3.4

Table 7: Fitted results of Gaussian parametrizations of the RQMD $\pi^+\pi^+$ and $\pi^-\pi^-$ correlation functions in Q_{TO}, Q_{TS} and Q_{L} ($\langle p_{\mathrm{T}} \rangle$ in MeV/c).

System	λ	R_{TO} (fm)	R_{TS} (fm)	R_{L} (fm)	χ^2/N
PbPb $\pi^-\pi^-$ (≈ 170)	0.58 ± 0.01	6.96 ± 0.14	6.23 ± 0.20	7.94 ± 0.21	1.38
PbPb $\pi^+\pi^+$ (≈ 170)	0.67 ± 0.01	6.43 ± 0.11	5.49 ± 0.14	7.68 ± 0.17	1.39
PbPb $\pi^+\pi^+$ (≈ 480)	0.92 ± 0.04	4.93 ± 0.17	3.92 ± 0.21	4.47 ± 0.22	1.35
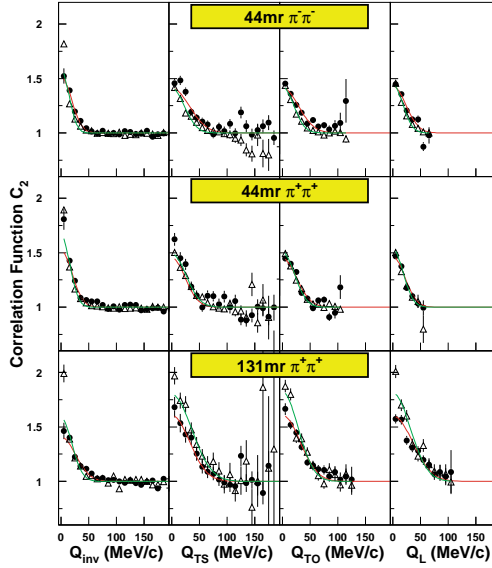
Figure 7: Comparison of NA44 data and RQMD predictions. The solid circles are the NA44 data and the open triangles are the RQMD predictions. The three-dimensional projections are averaged over the lowest 20 MeV/c in the other momentum differences.

The NA44 data does not show a statistically significant difference between π^+ and π^- correlation functions. In contrast, there is a significant difference between π^+ and π^- correlation functions in the RQMD calculations. The χ^2/N difference between the RQMD correlation functions for $|Q_{\mathrm{TS}}|, |Q_{\mathrm{TO}}|, |Q_{\mathrm{L}}| < 80$ MeV/c is 819/551. Since Coulomb interactions are not included in RQMD, this seems like a surprising result. The difference is caused by larger contributions of long-lived strange baryons and antibaryons (Λ, Σ, Ξ) to the π^- yield than to the π^+ yield. In this RQMD calculation, 30% of π^+ and 39% of π^- in the NA44 44-mrad acceptance come from decays of particles with lifetimes larger than 20 fm/c . This difference is most obvious in the lower value of the λ parameter for π^-. There are also slightly different values of the radius parameters for π^+ and π^- from RQMD. These are a consequence of extracting radius parameters from a fit which does not exactly fit the shape of the calculated correlation function. The RQMD calculation used the equivalent of 10^6 pairs in each setting for the 44 mrad case, while the NA44 data typically had about 10^5. Consequently, the calculation is more sensitive to π^+ and π^- differences.

12

It is important to understand the relationship between the size parameters from fits to a correlation function and the size of the source which produced the particles. As a useful tool in understanding this relationship, Fig. 8 shows the freeze-out position and time distributions of pions from RQMD. In these plots, x is defined as the Q_{TO} direction and y is along Q_{TS}. The beam direction is along the z axis. These plots are for positive pions and the horizontal focus setting of the spectrometer. The centroids and rms widths associated with the histograms in Fig. 8 are summarized in Table 8, which also contains the centroids and widths for the vertical focus setting of the spectrometer (not shown in Fig. 8).
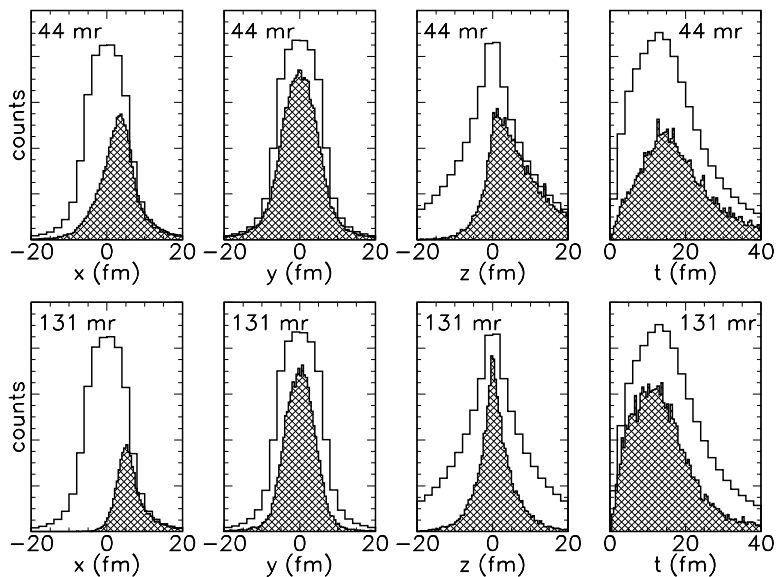

Figure 8: RQMD freeze-out distributions for pions. The unhatched histograms are for all pions from RQMD, and the hatched histograms are for pions in the NA44 44-mrad horizontal (upper panels) and 131-mrad horizontal (lower panels) acceptances. The x axis is in the direction of Q_{TO}, the y axis is in the Q_{TS} direction, and z is the beam axis. The centre-of-mass coordinate system is used.

The top part of Fig. 8 shows the position and time distributions of pions which contribute to the RQMD correlation function for the NA44 low-p_T setting and the bottom shows the corresponding distributions for the high-p_T setting. Each individual plot in Fig. 8 shows a histogram (solid line) which represents the distribution for all π^+ produced in an RQMD event, without an acceptance cut. These histograms are the same in the top (low p_T) and bottom (high p_T) halves of Fig. 8. The hatched histograms in each plot show the freeze-out distributions for pions which are in the NA44 low-p_T (top) and high-p_T (bottom) acceptances; these are the pions which were used to construct the RQMD correlation functions. In these plots, the relative normalizations of the plots with and without the acceptance cuts are arbitrary; only the shapes (and centroids) of the distributions should be compared.

A number of interesting observations can be made from Fig. 8. First, the freeze-out distributions of pions which contribute to the correlation functions are narrower than

the complete freeze-out distributions in all cases shown. Ideally, the size parameters from fitting the correlation functions should reflect the widths of the freeze-out distributions for pions within the acceptance. The size parameters should therefore be smaller than the full size of the source. From Fig. 8 we can also see that all of the distributions become narrower as p_T is increased, which is consistent with the experimental observation (and the RQMD result) in which the radius parameters get smaller with increasing p_T. Figure 8 also shows that the x position distribution (where x is in the direction of Q_{TO}) for particles in the acceptance is centred at positive x and that the centre of the distribution moves to large x values as p_T is increased. The HBT method only 'sees' the side of the source closest to it. This behaviour is qualitatively consistent with the position-momentum correlations in RQMD. It is also interesting that the widths of the distributions of particles in the two transverse directions (x and y) are not the same for particles in the acceptance. Formulas which attempt to calculate the duration of pion emission from the expression [6, 7, 19] $c\Delta\tau = \sqrt{(R_{TO}^2 - R_{TS}^2)}/\beta$ are based on the assumption that the 'true' size of the source in two transverse directions is the same. The size parameters measured by a correlation-function can (and in this case do) break this symmetry [20]. This is at least part of the reason that the duration of pion emission extracted from the above expression, when applied to the correlation-function fit parameters from RQMD, does not give the lifetime width values shown in Table 8: the values from the formula are significantly smaller than the actual duration of particle emission.

Table 8 also summarizes the position and time distributions for two simple acceptance models. The first model accepts all pions in the range $3.1 < y < 4.1$, $p_T < 400$ MeV/c, without an azimuthal cut. This is the range of rapidity and transverse momentum covered by the NA44 acceptance at 44 mrad. The numbers for this simple acceptance model are very similar to those within the NA44 horizontal and vertical focus acceptance at 44 mrad. Another simple acceptance model in Table 8, with $2.6 < y < 3.1$, $300 < p_T < 800$ MeV/c, and no azimuthal cut, covers the range of the NA44 131-mrad acceptance. Again, the results are similar to those for the NA44 acceptances at 131 mrad. This shows that the features seen in Fig. 8 are not caused by the details of the shape of the NA44 acceptance but should occur for any detector making measurements in this range of rapidity and transverse momentum.

It should be noted that a simple hadronic final-state rescattering model [23] is also able to reproduce the data equally as well as RQMD. RQMD includes final-state rescattering, so the primary difference in the two models is the initial conditions. In order to simultaneously reproduce the measured NA44 slope parameters [24] and pion interferometry results, however, the rescattering model requires that the initial temperature of the system is 222 MeV and that the initial baryon energy density is 1.48 GeV/fm^3 [23].

Table 8: The RQMD freeze-out distributions for pions, characterized by a mean value and σ (both in fm). 'All' refers to all pions from RQMD, H is the horizontal setting, and V is the vertical setting. Also shown are results for two ideal detectors which cover $3.1 < y < 4.1$, $p_T < 400$ MeV/c (an idealized version of the 44 mrad settings), and $2.5 < y < 3.1$, $300 < p_T < 800$ MeV/c (an idealized version of the 131 mrad settings). In the table, x is in the direction of Q_{TO} and y is in the direction of Q_{TS}.

	x		y		z		t	
	mean	σ	mean	σ	mean	σ	mean	σ
All	0.0	5.6	0.0	5.7	0.0	8.6	15.9	8.8
44 mrad H	2.7	5.0	0.0	5.1	4.3	5.6	17.2	7.5
44 mrad V	3.3	4.7	0.0	5.0	3.6	5.6	16.8	7.5
$3.1 < y < 4.1$, $p_T < 400$	2.8	4.9	0.0	5.2	3.9	5.9	17.0	7.5
131 mrad H	5.8	3.5	0.0	4.2	0.6	4.8	14.3	6.9
131 mrad V	5.9	3.4	0.1	4.2	0.0	4.6	14.3	6.7
$2.5 < y < 3.1$, $300 < p_T < 800$	5.6	3.5	0.0	4.3	-1.1	4.9	14.3	6.9

5 Conclusions

In summary, we have measured the first $\pi^+\pi^+$ and $\pi^-\pi^-$ correlations from collisions of Pb+Pb at high energy. The measured radius parameters are larger than the initial projectile, indicating a large amount of expansion before freeze-out. For example, the measured R_{TS} radius parameters using the Coulomb-wave correction ranged from 4.39 ± 0.31 fm (high-p_T π^+) to 5.87 ± 0.58 fm (low-p_T π^+). These are lower limits to the true size of the hot-dense region formed in the collision. In order to compare this to the radius of a Pb nucleus, the hard-sphere radius of Pb should be divided by $\sqrt{5}$ to give ≈ 3.2 fm. The R_L radius parameter follows the $1/\sqrt{m_T}$ scaling observed by NA44 for S+Pb collisions, but the R_{TO} radius parameter scales more weakly with increasing m_T. At low p_T the π^- and π^+ correlation functions are similar. The RQMD model is able to predict reasonably well both the shape of the correlation function and the fitted radius parameters.

References

[1] H. Beker et al. (NA44 Collaboration), Z. Phys. **C64**, 209 (1994);
H. Bøggild et al. (NA44 Collaboration), Phys. Lett. **B349**, 386 (1995);
K. Kaimi et al. (NA44 Collaboration), Z. Phys. **C75**, 619 (1997).

[2] Th. Alber et al. (NA35 Collaboration), Phys. Rev. Lett. **74**, 1303 (1995);
ibid. Z. Phys. **C66**, 77 (1995).

[3] D. Beavis et al., Phys. Rev. **C34**, 757 (1986).

[4] H. Bossy et al., Phys. Rev. **C47**, 1659 (1993).

[5] H Beker et al. (NA44 Collaboration), Phys. Rev. Lett. **74**, 3340 (1995).

[6] S. Pratt, Phys. Rev. **D33**, 1314 (1986).

[7] G. Bertsch and G.E. Brown, Phys. Rev. **C40**, 1830 (1989).

[8] D.E. Fields et al., Phys. Rev. **C52**, 986 (1995).

[9] B.R. Schlei and N. Xu, Phys. Rev. **C54**, R2155 (1996).

[10] S. Chapman and J.R. Nix, Phys. Rev. **C54**, 866 (1996).

[11] H. Beker et al. (NA44 Collaboration), Phys. Lett. **B302**, 510 (1993).

[12] N. Maeda et al., Nucl. Instrum. Methods **A346**, 132 (1994).

[13] C.W. Fabjan et al., Nucl. Instrum. Methods **A367**, 240 (1995);
A. Braem et al., CERN–PPE/97–120.

[14] S. Pratt, T. Csörgő and J. Zimányi, Phys. Rev. **C42**, 2646 (1990).

[15] W.A. Zajc et al., Phys. Rev. **C29**, 2173 (1984).

[16] S. Pratt, Phys. Rev. **D33**, 72 (1986).

[17] S. Chapman, P. Scotto, U. Heinz, Phys. Rev. Lett. **74**, 4400 (1995).

[18] B.R. Schlei, D. Strottman, N. Xu, Phys. Lett. **B420**, 1 (1998).

[19] S. Pratt and T. Csörgő, KFKI–1991–28A, 75.

[20] T. Csörgő and B. Lörstad, Phys. Rev. **C54**, 1390 (1996).

[21] J.P. Sullivan et al., Phys. Rev. Lett. **70**, 3000 (1993).

[22] H. Sorge, H. Stöcker, and W. Greiner, Nucl. Phys. **A498**, 567c (1989);
ibid. Ann. Phys. **192**, 266 (1989).

[23] T.J. Humanic, Phys. Rev. **C50**, 2525 (1994); ibid. **C53**, 901 (1996);
ibid. **C57**, 866 (1998).

[24] I.G. Bearden, et al., Phys. Rev. Lett. **78**, 2080 (1997).